

Theory of Spin-Acoustic Resonance for Spin-3/2 Si Vacancy with C_{3v} Site Symmetry in Silicon Carbide

Mikito Koga¹ and Masashige Matsumoto²

¹*Department of Physics, Faculty of Education, Shizuoka University, Shizuoka 422–8529, Japan*

²*Department of Physics, Faculty of Science, Shizuoka University, Shizuoka 422–8529, Japan*

Motivated by the recent acoustically driven spin resonance studies applied to silicon vacancy centers in silicon carbide, we theoretically investigate the spin–strain interaction characterized by the defect spin-3/2 quadrupole components coupled to strain fields. Considering the C_{3v} symmetry of the vacancy site beyond the spherical approximation, we clarify the effect of a deviation from the spherical symmetry on spin resonance transition rate, which can be changed by rotating a static magnetic field. The ratios of spin–strain coupling parameters can be evaluated from the anisotropic field-direction dependence of the transition rate using a standing or traveling surface acoustic wave. We also discuss the effect of the propagation direction of the acoustic wave tilted from the crystallographic mirror plane reflecting the C_{3v} symmetry. The results presented here reveal the quadrupole properties inherent in spin-3/2 states and will promote the realization of the acoustically driven strain control of spin.

1. Introduction

High spin ($S \geq 1$) states can be coupled to strain fields driven by acoustic waves or mechanical oscillators.^{1–3} The mechanical control of spin provides another possibility of quantum spin control at the nanoscale, as extensively studied using optically and magnetically controlled spin systems such as the nitrogen-vacancy (NV) centers in diamond.^{3–17} The silicon vacancy (V_{Si}) centers in silicon carbide (SiC) are considered leading platforms for spin–strain coupling with high sensitivity to realize the acoustic control of quantum spin states, which can be considered an alternative to spin manipulation by microwaves.^{18–21} Unlike the NV spin-1 defect, the higher spin $S = 3/2$ of V_{Si} causes more complicated spin dynamics, and it is highly desirable to clarify the details of an acoustically driven spin–strain interaction with the C_{3v} site symmetry of V_{Si} .^{22–32}

Recently, spin-acoustic resonance (SAR) measurements in 4H-SiC have shown that phonon-driven quantum spin resonance transitions depend on the rotation of a static magnetic field on the SiC surface.³³ The SAR is driven by single and double quantum spin transitions between two different $S = 3/2$ energy levels m_S with $\Delta m_S = \pm 1$ and $\Delta m_S = \pm 2$. Although the data analysis is based on a spherically symmetric spin–strain interaction model,^{27,34} it is important that an observed nontrivial field-direction dependence should reflect the symmetries of $S = 3/2$ quadrupole components coupled to strain fields driven by a surface acoustic wave (SAW). This is a key to our theory considering the C_{3v} site symmetry of a defect spin beyond the spherical approximation, which was previously proposed for phonon-driven resonance in the NV centers.^{35,36}

In this paper, we present a useful representation of the spin–strain interaction for the V_{Si} spin $S = 3/2$ under the rotation of a magnetic field and derive a fundamental formulation for the single quantum spin transition rate with $\Delta m_S = \pm 1$. The anisotropic SAR depends on the local strain fields coupled to defect spins as well as the spin–strain coupling parameters for C_{3v} . We focus on the ratios of coupling strengths, which are essential for reproducing the field-direction dependence

of SAR. This is an advantage of our method for analyzing the anisotropic SAR data affected by various strain-field amplitudes. The evaluated coupling-strength ratios can be compared straightforwardly with those assessed by other methods such as first-principles calculation.

This paper is organized as follows. In Sect. 2, a model Hamiltonian is introduced to describe the spin–strain interaction with the C_{3v} site symmetry using quadrupole operators (second-rank tensorial forms of spin operators). Under the rotation of a strong magnetic field, we investigate the SAR transitions between the two lowest-lying $S = 3/2$ levels coupled to local strain fields, which are driven by a standing or traveling SAW. In Sect. 3, we demonstrate how to evaluate the spin–strain coupling parameters for C_{3v} from the field-direction dependence of SAR transition rate, considering a deviation of the parameters from the spherical symmetry as well. The effect of the SAW propagating in general directions is also discussed. In particular, we demonstrate how the anisotropic C_{3v} symmetry appears in the transition rate. For this purpose, we also study the double quantum spin ($\Delta m_S = \pm 2$) transition rate. In the last section, we present the conclusion of this paper. In Appendix A, we explicitly show the matrix forms of spin and quadrupole operators for $S = 3/2$. The unitary transformation of these operators is also given in the case of the rotation of a magnetic field. In Appendix B, we describe a spherically symmetric spin–strain interaction model for comparison. Appendix C shows our formulation of the double quantum spin transition rate.

2. Model and Formulation

2.1 Spin–strain interaction driven by SAW

To describe the coupling between the electronic spin and strain components due to elastic deformations, we study the following form of the spin–strain interaction Hamiltonian:

$$H_\varepsilon = \sum_k A_{k,\varepsilon} O_k \quad (k = u, v, zx, xy, yz), \quad (1)$$

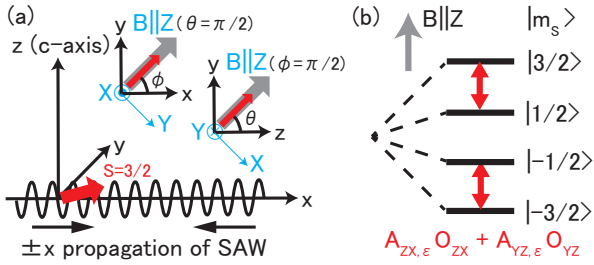


Fig. 1. (Color online) (a) Illustration of V_{Si} defect spin ($S = 3/2$) coupled to the $\pm x$ propagating SAWs in the SiC surface layer perpendicular to the crystallographic axis $c \parallel z$. The applied magnetic field $\mathbf{B} = B(\sin \theta \cos \phi, \sin \theta \sin \phi, \cos \theta)$ is rotated in the xy ($\theta = \pi/2$) and yz ($\phi = \pi/2$) planes. (b) Level splitting for a sufficiently strong magnetic field B . The two levels are coupled via the ZX and YZ quadrupole components in the single quantum spin transition.

where the five quadrupole operators O_K are constructed by the vector of spin operators $\mathbf{S} = (S_x, S_y, S_z)$ as

$$\begin{aligned} O_u &= \frac{1}{\sqrt{3}}(2S_z^2 - S_x^2 - S_y^2) = \frac{1}{\sqrt{3}}[3S_z^2 - S(S+1)], \\ O_v &= S_x^2 - S_y^2, \quad O_{zx} = S_z S_x + S_x S_z, \\ O_{xy} &= S_x S_y + S_y S_x, \quad O_{yz} = S_y S_z + S_z S_y. \end{aligned} \quad (2)$$

The coupling with each quadrupole is expressed by the strain-dependent coupling coefficient $A_{k,\varepsilon}$. In the C_{3v} reference frame at the spin site, the spin-strain interaction is characterized by^{3,37)}

$$\begin{aligned} A_{u,\varepsilon} &= \frac{h_a}{4}\varepsilon_u, \quad A_{v,\varepsilon} = \frac{1}{2}\left(\frac{1}{2}h_b\varepsilon_v - h_c\varepsilon_{zx}\right), \\ A_{zx,\varepsilon} &= \frac{1}{2}\left(-\frac{1}{2}h_{b'}\varepsilon_v + h_{c'}\varepsilon_{zx}\right), \quad A_{xy,\varepsilon} = \frac{1}{2}(h_b\varepsilon_{xy} + h_c\varepsilon_{yz}), \\ A_{yz,\varepsilon} &= \frac{1}{2}(h_{b'}\varepsilon_{xy} + h_{c'}\varepsilon_{yz}), \end{aligned} \quad (3)$$

where $\{\varepsilon_{\alpha\beta}\}$ ($\alpha, \beta = x, y, z$) are strain components, $\varepsilon_u = (2\varepsilon_{zz} - \varepsilon_{xx} - \varepsilon_{yy})/\sqrt{3}$, $\varepsilon_v = \varepsilon_{xx} - \varepsilon_{yy}$, and a bulk strain component is disregarded. There are five independent coupling parameters h_λ ($\lambda = a, b, c, b', c'$). As shown in Fig. 1(a), we consider a plane Rayleigh SAW propagating in either the $+x$ or $-x$ direction, oscillating in the z and x directions (no displacement along y). In this case, only A_u , A_v , and A_{zx} are taken into account because the strain components are restricted to ε_{xx} , ε_{zz} , and ε_{zx} ($\varepsilon_{yy} = \varepsilon_{yz} = \varepsilon_{xy} = 0$) here. This simplification does not hold when the direction of SAW propagation deviates from a mirror (zx) plane, which will be discussed in Sect. 3.6.

2.2 Spin-strain interaction under rotation of a static magnetic field

The $S = 3/2$ ground state of V_{Si} is split into the $m_S = \pm 1/2$ and $m_S = \pm 3/2$ Kramers doublets in the C_{3v} crystal-field environment. In the presence of a magnetic field \mathbf{B} , the local spin Hamiltonian is $H_B = g\mu_B \mathbf{S} \cdot \mathbf{B} + DO_u/\sqrt{3}$, where g is the electron g -factor, μ_B is the Bohr magneton, and $2D$ equals the zero field splitting. The field direction is represented by two angles θ and ϕ as $\mathbf{B}/B = (\sin \theta \cos \phi, \sin \theta \sin \phi, \cos \theta)$. We now consider the case $g\mu_B B \gg D$ and neglect the mixing

of the $S = 3/2$ quartet states as shown in Fig. 1(b).³³⁾ This allows us to rotate the \mathbf{B} direction without changing the Zeeman energy shift.

We next introduce a new reference frame (XYZ) where Z is chosen along the \mathbf{B} direction and define the Z -axis unit vector as $\mathbf{e}_Z = (\sin \theta \cos \phi, \sin \theta \sin \phi, \cos \theta)$. For the other orthogonal axes, we define $\mathbf{e}_X = (-\cos \theta \cos \phi, -\cos \theta \sin \phi, \sin \theta)$ and $\mathbf{e}_Y = (\sin \phi, -\cos \phi, 0)$. For the (XYZ) frame, we transform the spin operators from $\mathbf{S} = (S_x, S_y, S_z)$ to $\mathbf{S}_B = (S_X, S_Y, S_Z)$ as $U^\dagger(\mathbf{e}_\lambda \cdot \mathbf{S})U = S_\lambda$ ($\lambda = X, Y, Z$), using the unitary matrix U for spin-3/2 in Appendix A. For an electronic spin coupled to elastic strains, the quantum spin transitions between the $S = 3/2$ states are described by the quadrupole operators O_K in Eq. (2). Under a magnetic field, it is convenient to use the quadrupole operators in the (XYZ) frame. By the unitary transformation, we transform Eq. (1) to

$$H_{\varepsilon,B} = U^\dagger H_\varepsilon U \equiv \sum_K A_{K,\varepsilon} O_K, \quad (4)$$

where the quadrupole operators O_K ($K = U, V, ZX, XY, YZ$) are constructed by the components of \mathbf{S}_B . For the finite strain components ε_{xx} , ε_{zz} , and ε_{zx} of the SAW considered here, the field-direction-dependent coupling coefficients $A_{K,\varepsilon}$ are given by linear combinations of $A_{u,\varepsilon}$, $A_{v,\varepsilon}$, and $A_{zx,\varepsilon}$ in Eq. (3). For the single quantum spin transition with $\Delta m_S = \pm 1$ in Fig. 1(b), they are represented as

$$\begin{aligned} A_{ZX,\varepsilon} &= A_{u,\varepsilon} \cdot \sqrt{3} \sin \theta \cos \theta + A_{v,\varepsilon}(-\sin \theta \cos \theta) \cos 2\phi \\ &\quad + A_{zx,\varepsilon}(-\cos 2\theta) \cos \phi, \\ A_{YZ,\varepsilon} &= A_{v,\varepsilon} \sin \theta \sin 2\phi + A_{zx,\varepsilon} \cos \theta \sin \phi, \end{aligned} \quad (5)$$

whereas A_U , A_V , and A_{ZX} are not involved in Eq. (4). Hence, the spin-strain interaction is described by $H = BS_Z + H_{\varepsilon,B}$ in the presence of a magnetic field.

2.3 Single quantum spin transition driven by SAW

For the strain components driven by a SAW, we adopt a realistic assumption that ε_{xx} and ε_{zz} are real, whereas $\varepsilon_{zx} \equiv -i\varepsilon'_{zx}$ is purely imaginary (ε''_{zx} is real).³³⁾ Accordingly, A_u is real and the other components are represented by $A_v = |A_v|e^{i\theta_v}$ and $A_{zx} = |A_{zx}|e^{i\theta_{zx}}$, where the subscripts ε of $A_{k,\varepsilon}$ are omitted. From this representation, the coupling parameters in Eq. (3) are also related to A_v and A_{zx} as

$$\begin{aligned} \frac{h_b}{4}\varepsilon_{xx} &= |A_v| \cos \theta_v, \quad \frac{h_c}{2}\varepsilon''_{zx} = |A_v| \sin \theta_v, \\ -\frac{h_{b'}}{4}\varepsilon_{xx} &= |A_{zx}| \cos \theta_{zx}, \quad -\frac{h_{c'}}{2}\varepsilon''_{zx} = |A_{zx}| \sin \theta_{zx}. \end{aligned} \quad (6)$$

In a spherical approximation, $h_a = h_b = h_{c'}$ and $h_c = h_{b'} = 0$; the latter indicates $\theta_v = 0$ and $|\theta_{zx}| = \pi/2$. As noted in Appendix B, we have $\tan \theta_v / \tan \theta_{zx} = (h_c h_{b'}) / (h_b h_{c'})$, which represents a deviation from the spherical symmetry. In general, θ_v and θ_{zx} change satisfying $0 \leq |\theta_v|, |\theta_{zx}| \leq \pi$.

In Fig. 1(b), we restrict ourselves to the two lowest-lying states $|g\rangle = |m_S = -3/2\rangle$ and $|e\rangle = |m_S = -1/2\rangle$ to calculate the transition matrix element $M = \langle e|A_{ZX,\varepsilon}O_{ZX} + A_{YZ,\varepsilon}O_{YZ}|g\rangle$. In SAR measurements, V_{Si} centers can be coupled simultaneously to two SAWs propagating along the $+x$ and $-x$ directions with intensities I_+ and I_- , respectively. The transition rate between the $|g\rangle$ and $|e\rangle$ states is proportional to the sum

of the SAW contributions,

$$W \propto \left\langle |M_+|^2 \frac{I_+}{I_+ + I_-} + |M_-|^2 \frac{I_-}{I_+ + I_-} \right\rangle, \quad (7)$$

where the transition matrix elements M_+ and M_- are related to $+x$ and $-x$ propagations, respectively, and M_- is given by replacing $\varepsilon''_{zx} \rightarrow -\varepsilon''_{zx}$ ($\theta_v \rightarrow -\theta_v$ and $\theta_{zx} \rightarrow -\theta_{zx}$) in M_+ .³³⁾ The bracket $\langle \dots \rangle$ indicates the average of the strain amplitudes along x (surface layer) and z (depth) considering the spatial distribution of V_{Si} centers.

3. Results

3.1 Field-direction-dependent transition rate

First, we consider the transition matrix element $M_{xy,\pm}$ for the inplane (xy) rotation of $\mathbf{B} = B(\cos \phi, \sin \phi, 0)$, where $\theta = \pi/2$. Using Eq. (5), we obtain

$$M_{xy,\pm} = \sqrt{3}|A_v|[-|a_{zx}|e^{\pm i(\theta_{zx}-\theta_v)} \cos \phi + i \sin 2\phi], \quad (8)$$

with $a_{zx} = A_{zx}/|A_v|$. The transition rate is calculated as

$$W_{xy} \propto \left\langle 3|A_v|^2 [|a_{zx}|^2 \cos^2 \phi + \sin^2 2\phi - 2\eta|a_{zx}| \sin(\theta_{zx} - \theta_v) \cos \phi \sin 2\phi] \right\rangle, \quad (9)$$

where the parameter $\eta = (I_+ - I_-)/(I_+ + I_-)$ represents a standing wave for $\eta = 0$ and a one-way traveling wave for $\eta = \pm 1$. The intermediate case $0 < |\eta| < 1$ represents different weights of combined counterpropagating SAWs. The last term in Eq. (9) indicates the difference between the C_{3v} symmetry and the spherical approximation. This enables us to evaluate the coupling parameters in the spin-strain interaction from experimental results as discussed below.

The values of $\langle |a_{zx}| \rangle$ and $\Delta\theta \equiv \theta_{zx} - \theta_v$ can be determined from W_{xy} as a function of ϕ . From these values, we can evaluate the coupling-strength ratios $h_{b'}/h_b$ and $h_{c'}/h_c$ in Eq. (6). In this study, we pay attention to the maximum transition rate W_{xy} for $\eta = 0$ and $|\eta| = 1$, assuming that the combination of $\pm x$ propagating SAWs can be controlled by adjusting the edge reflection.

3.2 Transition rate W_{xy} for $\eta = 0$

In Eq. (9), we consider W_{xy} as a function of $\langle |a_{zx}| \rangle$ to simplify the calculation of the maximums, assuming that $\langle |a_{zx}| \rangle$ is substituted for $\sqrt{\langle |a_{zx}|^2 \rangle}$. For $\eta = 0$, the maximum $W_{xy,\max}$ is obtained for $\phi = (1/2) \arccos(\langle |a_{zx}|^2 \rangle / 4)$. We then introduce the quantity

$$w_{xy,0}^2 \equiv \left(\frac{W_{xy,\max} - W_{xy,\phi=0}}{W_{xy,\phi=0}} \right)_{\eta=0} = \frac{1}{\langle |a_{zx}|^2 \rangle} \left(1 - \frac{\langle |a_{zx}|^2 \rangle}{4} \right)^2 \quad (10)$$

and solve

$$\langle |a_{zx}| \rangle = 2 \left(-w_{xy,0} + \sqrt{1 + w_{xy,0}^2} \right). \quad (11)$$

In Fig. 2(a), W_{xy} is plotted for $\langle |a_{zx}| \rangle = \sqrt{\langle |a_{zx}|^2 \rangle} = 0.5$. A measurable value of $w_{xy,0}^2$ determines $\langle |a_{zx}| \rangle$ in Eq. (11). Figure 2(b) shows the polar representation of $W_{xy}/W_{xy,\phi=0}$ as a function of ϕ for various values of $\langle |a_{zx}| \rangle$. The contours of the plots are symmetric with respect to the inversion of B_x (for instance, $\phi \rightarrow \pi - \phi$) owing to a mirror plane of zx and the inversion of B_y ($\phi \rightarrow 2\pi - \phi$) owing to the time-reversal symmetry for $\eta = 0$.³³⁾ For small values of $\langle |a_{zx}| \rangle < 1$, W_{xy} shows four

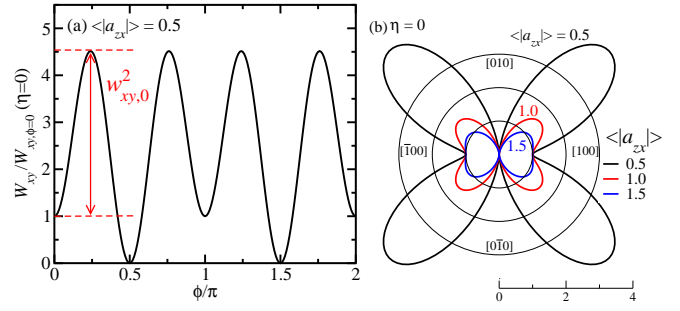


Fig. 2. (Color online) (a) Transition rate for the standing SAW ($\eta = 0$) plotted as a function of the field-rotation angle ϕ in the xy plane for $\langle |a_{zx}| \rangle = 0.5$. A measurable value of $w_{xy,0}^2$ indicated by the two-headed arrow is used for calculating $\langle |a_{zx}| \rangle$. (b) Polar representation of the normalized rate plotted as the radius coordinate with respect to ϕ for $\langle |a_{zx}| \rangle = 0.5, 1.0$, and 1.5 .

peaks at $\phi/\pi \simeq 1/4, 3/4, 5/4$, and $7/4$, which are markedly increased by a large deviation from the spherical symmetry at $\langle |a_{zx}| \rangle \simeq 1$ in the spin-strain interaction.

For the spherical model in Eq. (B·1), $\langle |a_{zx}| \rangle$ only depends on $2\langle \varepsilon''_{zx}\varepsilon_{xx} \rangle / \langle \varepsilon_{xx}^2 \rangle$. According to an estimate for the SAR measurements,³³⁾ this value approximately equals 1.2. For $\langle |a_{zx}| \rangle > 1$, W_{xy} does not exhibit the V-shaped angular dependence at $\phi = 0$ and π as shown in Fig. 2(b), whereas the V-shaped dependence is found in the SAR data.³³⁾ This discrepancy can be solved by considering a deviation from the spherical symmetry $|h_{c'}/h_b| < 1$ for C_{3v} . Indeed, we can estimate $w_{xy,0}^2 \simeq 2$ from the SAR data and obtain $\langle |a_{zx}| \rangle \simeq 0.6$ from Eq. (11).

3.3 Transition rate W_{xy} for $|\eta| = 1$

The above procedure is also applied to W_{xy} for $|\eta| = 1$. Similarly, we define

$$\begin{aligned} w_{xy,1}^2 &\equiv \left(\frac{W_{xy,\max} - W_{xy,\phi=0}}{W_{xy,\phi=0}} \right)_{|\eta|=1} \\ &= \langle |a_{zx}|^2 \rangle^{-1} \left(\langle |a_{zx}|^2 \rangle \cos^2 \phi_{\max} + \sin^2 2\phi_{\max} \right. \\ &\quad \left. + 2\gamma_{xy} \langle |a_{zx}| \rangle \cos \phi_{\max} \sin 2\phi_{\max} \right) - 1 \\ &(\gamma_{xy} \equiv |\sin(\theta_{zx} - \theta_v)|). \end{aligned} \quad (12)$$

Here, ϕ_{\max} is the angle for a maximum $W_{xy,\max}$. Using the value of $\langle |a_{zx}| \rangle$ evaluated from Eq. (11), we obtain the parameter γ_{xy} from the measurable values of $w_{xy,1}$ and ϕ_{\max} . In Fig. 3(a), W_{xy} is plotted for $\eta = -1$, where $\Delta\theta \equiv \theta_{zx} - \theta_v = 0.5\pi$ is fixed. The value of $\gamma_{xy} \equiv |\sin \Delta\theta|$ can be evaluated from Eq. (12) with the measurable values of $w_{xy,1}$ and ϕ_{\max} . Figure 3(b) shows the polar plots of $W_{xy}/W_{xy,\phi=0}$ for various values of $\Delta\theta$. The asymmetric contours of the plots ($W_{xy,\phi} \neq W_{xy,-\phi}$) are due to the broken time-reversal symmetry for $\eta \neq 0$. Note that the maximum transition rate decreases with decreasing in $\Delta\theta/\pi$ from 0.5. The symmetric ϕ dependence in Fig. 2(b) is restored at $\Delta\theta = 0$ even for $\eta \neq 0$ owing to the disappearance of the last term in Eq. (9). It is the special case $\theta_v = \theta_{zx}$ for C_{3v} where the coupling parameters satisfy $h_{b'}/h_b = h_{c'}/h_c$ in Eq. (6).

For the spherical model in Eq. (B·1), the ϕ dependence for $|\eta| = 1$ corresponds to $\Delta\theta/\pi = 0.5$ because of $\theta_v = 0$ ($h_c = 0$) and $\theta_{zx}/\pi = 0.5$ ($h_{b'} = 0$) as shown in Fig. B·1(b). For a

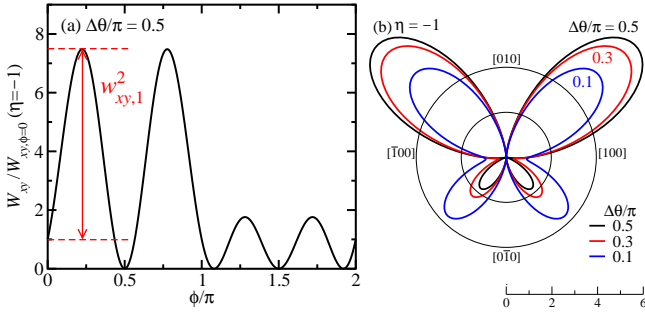


Fig. 3. (Color online) (a) Transition rate for the $-x$ propagating SAW ($\eta = -1$) plotted as a function of ϕ for $\Delta\theta \equiv \theta_{zx} - \theta_v = 0.5\pi$. Here, we fix $\langle |a_{zx}| \rangle = 0.5$. The measurable value $w_{xy,1}^2$ indicated by the two-headed arrow is used for evaluating θ_v and θ_{zx} . (b) Polar representation of the normalized transition rate for $\Delta\theta/\pi = 0.5, 0.3$, and 0.1 .

large deviation $|\Delta\theta/\pi| \ll 0.5$ from the spherical symmetry, the ϕ dependence becomes symmetric as shown for $\eta = 0$ in Fig. 2(b).

3.4 Transition rate under inplane (yz) field rotation

To determine θ_v and θ_{zx} , we apply a similar formulation to a different spin transition rate W_{yz} for the inplane (yz) rotation of $\mathbf{B} = B(0, \sin\theta, \cos\theta)$, where $\phi = \pi/2$. As given by Eqs. (10) and (12), we can express

$$w_{yz,0}^2 \equiv \left(\frac{W_{yz,\max} - W_{yz,\theta=0}}{W_{yz,\theta=0}} \right)_{\eta=0} = \frac{\langle \alpha_u^2 \rangle}{\langle 4|a_{zx}|^2 \rangle} \left(1 - \frac{\langle |a_{zx}|^2 \rangle}{\langle \alpha_u^2 \rangle} \right)^2$$

$$(\alpha_u^2 \equiv 3a_u^2 + 2\sqrt{3}a_u \cos\theta_v + 1, a_u = A_u/|A_v|), \quad (13)$$

and

$$w_{yz,1}^2 \equiv \left(\frac{W_{yz,\max} - W_{yz,\theta=0}}{W_{yz,\theta=0}} \right)_{|\eta|=1}$$

$$= \langle |a_{zx}|^2 \rangle^{-1} \left(\langle |a_{zx}|^2 \rangle \cos^2 \theta_{\max} + \frac{\langle \alpha_u^2 \rangle}{4} \sin^2 2\theta_{\max} \right. \\ \left. + 2\gamma_{yz} \langle |a_{zx}| \rangle \cos \theta_{\max} \sin 2\theta_{\max} \right) - 1$$

$$(2\gamma_{yz} \equiv |\sqrt{3}\langle a_u \rangle \sin \theta_{zx} + \sin(\theta_{zx} - \theta_v)|). \quad (14)$$

Here, θ_{\max} is the angle for a maximum $W_{yz,\max}$ ($|\eta| = 1$). From Eq. (13), we obtain

$$\langle \alpha_u^2 \rangle = \langle |a_{zx}|^2 \rangle \left(-w_{yz,0} + \sqrt{1 + w_{yz,0}^2} \right)^{-2}, \quad (15)$$

with the measurable value $w_{yz,0}$ and the $\langle |a_{zx}| \rangle$ determined using Eq. (10). The parameter γ_{yz} can be determined from the measurable values of $w_{yz,1}$ and θ_{\max} , where $\langle |a_{zx}| \rangle$ and $\langle \alpha_u^2 \rangle$ are already known. In Table I, we summarize the measurable and evaluated quantities for the coupling parameters in the spin-strain interaction. The parameters $\langle |a_{zx}| \rangle$, $\langle \alpha_u^2 \rangle$, γ_{xy} , and γ_{yz} are used for evaluating the coupling-strength ratios h_b/h_c and h_c/h_c in the spin-strain interaction for C_{3v} , which will be discussed in the next subsection.

3.5 Evaluation of coupling-strength ratios of spin-strain interaction

Now, γ_{xy} and γ_{yz} are determined from the measurable values. From Eq. (6), it is convenient to introduce the following

Table I. List of measurable and calculated quantities for the evaluation of the coupling parameters. The values of $w_{xy,0}$, $w_{xy,1}$, and ϕ_{\max} are obtained from the ϕ dependence of the single quantum spin transition rate W_{xy} in the xy plane, and those of $w_{yz,0}$, $w_{yz,1}$, and θ_{\max} are obtained from the θ dependence of W_{yz} in the yz plane. The values of $\langle |a_{zx}| \rangle$, γ_{xy} , $\langle \alpha_u^2 \rangle$, and γ_{yz} in the second column are calculated from the measurable values listed in the first column. In the third column, $|\eta| = 0$ and $|\eta| = 1$ represent the standing and traveling SAWs propagating along the x -axis, respectively.

Measurable	Calculated	$ \eta $ (SAW)
$w_{xy,0}$	$\langle a_{zx} \rangle$	0
$w_{xy,1}, \phi_{\max}$	γ_{xy} using $\langle a_{zx} \rangle$	1
$w_{yz,0}$	$\langle \alpha_u^2 \rangle$ using $\langle a_{zx} \rangle$	0
$w_{yz,1}, \theta_{\max}$	γ_{yz} using $\langle a_{zx} \rangle$ and $\langle \alpha_u^2 \rangle$	1

parameters:

$$r_b \equiv \frac{\cos \theta_{zx}}{\cos \theta_v} = -\frac{h_b'}{h_b} \langle |a_{zx}| \rangle, \quad r_c \equiv \frac{\sin \theta_{zx}}{\sin \theta_v} = -\frac{h_c'}{h_c} \langle |a_{zx}| \rangle, \quad (16)$$

which are given by Eq. (6). To evaluate the coupling-strength ratios h_b'/h_b and h_c'/h_c , we determine r_b and r_c from the values of γ_{xy} and γ_{yz} as follows. Here, let us change θ_v and θ_{zx} under the condition $\theta_v + \theta_{zx} = \theta_0$ ($0 \leq \theta_v < \theta_0/2 \leq \pi/4$), and rewrite r_b and r_c as

$$r_b \equiv \frac{\cos \theta_{zx}}{\cos \theta_v} = \cos \theta_0 + \sin \theta_0 \tan \theta_v \quad (\cos \theta_0 \leq r_b \leq 1), \quad (17)$$

$$r_c \equiv \frac{\sin \theta_{zx}}{\sin \theta_v} = -\cos \theta_0 + \frac{\sin \theta_0}{\tan \theta_v} \quad (r_c \geq 1). \quad (18)$$

Eliminating $\tan \theta_v$, we obtain

$$r_b = \frac{r_c^{-1} + \cos \theta_0}{1 + r_c^{-1} \cos \theta_0} \quad (0 \leq r_c^{-1} \leq 1). \quad (19)$$

On the other hand, r_b and r_c satisfy $r_b^2 \cos^2 \theta_v + r_c^2 \sin^2 \theta_v = 1$, which leads to

$$\sin^2 \theta_v = \frac{1 - r_b^2}{r_c^2 - r_b^2} = r_c^{-2} \left[1 + \frac{r_b^2(r_c^2 - 1)}{r_c^2(1 - r_b^2)} \right]^{-1}, \quad \cos^2 \theta_v = \frac{r_c^2 - 1}{r_c^2 - r_b^2},$$

$$\sin^2(\theta_{zx} - \theta_v) = (\sin \theta_{zx} \cos \theta_v - \cos \theta_{zx} \sin \theta_v)^2$$

$$= (r_c \sin \theta_v \cos \theta_v - r_b \cos \theta_v \sin \theta_v)^2$$

$$= (r_c - r_b)^2 \sin^2 \theta_v \cos^2 \theta_v = \frac{(1 - r_b^2)(r_c^2 - 1)}{(r_b + r_c)^2}$$

$$= \left[1 + \frac{(1 + r_b r_c)^2}{(1 - r_b^2)(r_c^2 - 1)} \right]^{-1}. \quad (20)$$

Combining Eqs. (19) and (20), we obtain

$$\gamma_{xy} = \frac{(1 - r_c^{-2}) \sin \theta_0}{\{(1 - r_c^{-2})^2 \sin^2 \theta_0 + [2r_c^{-1} + (1 + r_c^{-2}) \cos \theta_0]^2\}^{1/2}} \quad (21)$$

and

$$\gamma_{yz} = \frac{1}{2} \left| \frac{\sqrt{3}\langle a_u \rangle \sin \theta_0}{[(r_c^{-1} + \cos \theta_0)^2 + \sin^2 \theta_0]^{1/2}} + \gamma_{xy} \right|, \quad (22)$$

as a function of r_c^{-1} ($0 \leq r_c^{-1} \leq 1$). Here, $\langle a_u \rangle$ is related to $\langle \alpha_u^2 \rangle$ in Eq. (13), and the latter is calculated from the measurable value of $w_{yz,0}$. In Figs. 4(a) and 4(b), we show the r_c^{-1} dependences of γ_{xy} and γ_{yz} , respectively. We can extract r_c^{-1} and θ_0 to reproduce the observed values of γ_{xy} and γ_{yz} shown in Ta-

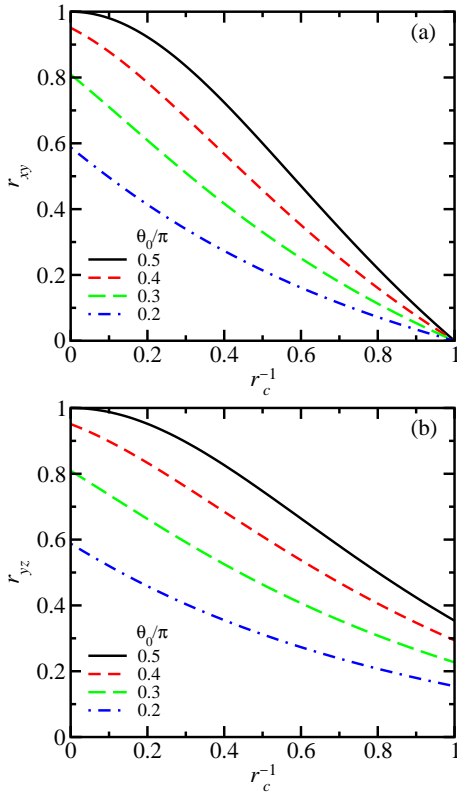


Fig. 4. (Color online) (a) Plots of the parameter γ_{xy} as a function of $r_c^{-1} \equiv \sin \theta_v / \sin \theta_{zx}$ for various values of $\theta_0 = \theta_v + \theta_{zx}$, related to the transition rate W_{xy} under the rotation of a magnetic field in the xy plane. (b) Plots of γ_{yz} as a function of r_c^{-1} , where $\sqrt{3}\langle a_{ii} \rangle = 1$ is used, related to W_{yz} under the rotation of a magnetic field in the yz plane. The spherical spin–strain coupling case corresponds to $\gamma_{xy} = \gamma_{yz} = 1$ at $r_c^{-1} = 0$.

ble I. As a result, we obtain r_b using Eq. (19). Finally, we can determine $h_{b'}/h_b$ and $h_{c'}/h_c$ using r_b and r_c with the value of $\langle |a_{zx}| \rangle$ in Eq. (16).

For the NV centers in diamond, the coupling strengths $|h_{b'}|$ and $|h_{c'}|$ are related to the zx and yz quadrupole components as shown in Eq. (3). They have been considered negligibly small in earlier studies,^{15,38)} whereas it was reported that $h_{b'}/h_b \simeq -0.46$ and $h_{c'}/h_c \simeq -0.14$ were assessed by the first-principles calculation.³⁾ In addition, recent acoustic measurements indicated a relatively large spin–stress coupling strength related to $h_{b'}$ and $h_{c'}$.¹⁶⁾ It does not seem so difficult to probe the quantum spin transitions driven by the zx and yz quadrupole components; however, this has not been established for the NV centers yet.

3.6 SAW propagating in general directions

Here, we demonstrate how W_{xy} is affected by the SAW propagation direction deviating from the crystallographic axis. We choose the x' -axis along the SAW propagation direction and introduce a new reference frame ($x'y'z$) obtained by the transformation

$$\begin{pmatrix} x' \\ y' \end{pmatrix} = \begin{pmatrix} \cos \varphi & \sin \varphi \\ -\sin \varphi & \cos \varphi \end{pmatrix} \begin{pmatrix} x \\ y \end{pmatrix}. \quad (23)$$

Here, the x' -axis is rotated from x by angle φ . As in the $\varphi = 0$ case, the finite strain components are restricted to $\varepsilon_{x'x'}$ and $\varepsilon_{x'z}$ for the SAWs (no displacement along y'). In Eq. (3), the

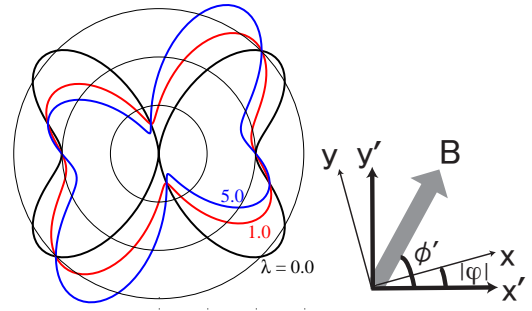


Fig. 5. (Color online) Polar representation of normalized transition rate $W_{xy,0}/W_{xy,0,\phi'=0}$ for $\eta = 0$ plotted as a function of ϕ' for $\lambda = 0.0, 1.0,$ and 5.0 in Eq. (29), where $\varphi = -\pi/12$ is used. The angle ϕ' is the \mathbf{B} direction measured from the SAW propagation axis (x' -axis).

strain tensor components $\{\varepsilon_{xx}, \varepsilon_{yy}, \varepsilon_{xy}, \varepsilon_{zx}, \varepsilon_{yz}\}$ are replaced as follows:

$$\begin{aligned} \varepsilon_{xx} &\rightarrow \varepsilon_{x'x'} \cos^2 \varphi, & \varepsilon_{yy} &\rightarrow \varepsilon_{x'x'} \sin^2 \varphi, & \varepsilon_{xy} &\rightarrow \varepsilon_{x'x'} \sin \varphi \cos \varphi, \\ \varepsilon_{zx} &\rightarrow \varepsilon_{x'z} \cos \varphi, & \varepsilon_{yz} &\rightarrow \varepsilon_{x'z} \sin \varphi. \end{aligned} \quad (24)$$

In the (XYZ) frame for a finite \mathbf{B} , we use the unitary transformation in Eq. (A-6) for $\theta = \pi/2$ and obtain the field-direction-dependent coupling coefficients,

$$\begin{aligned} A_{ZX,\varepsilon} &= \frac{1}{2} \left[h_{c'} \varepsilon_{x'z} \cos \varphi - \frac{1}{2} h_b \varepsilon_{x'x'} (\cos^2 \varphi - \sin^2 \varphi) \right] \cos \phi \\ &\quad + \frac{1}{2} [h_{c'} \varepsilon_{x'z} \sin \varphi + h_b \varepsilon_{x'x'} \sin \varphi \cos \varphi] \sin \phi, \end{aligned} \quad (25)$$

$$\begin{aligned} A_{YZ,\varepsilon} &= \frac{1}{2} \left[-h_c \varepsilon_{x'z} \cos \varphi + \frac{1}{2} h_b \varepsilon_{x'x'} (\cos^2 \varphi - \sin^2 \varphi) \right] \sin 2\phi \\ &\quad - \frac{1}{2} [h_c \varepsilon_{x'z} \sin \varphi + h_b \varepsilon_{x'x'} \sin \varphi \cos \varphi] \cos 2\phi, \end{aligned} \quad (26)$$

for the ZX and YZ quadrupole components, respectively. We obtain the transition matrix elements $M_{\pm} = \langle e | A_{ZX,\varepsilon} O_{ZX} + A_{YZ,\varepsilon} O_{YZ} | g \rangle$ for $\varepsilon_{x'z} = \mp i \varepsilon_{x'z}''$ ($\varepsilon_{x'z}$ is purely imaginary):

$$\begin{aligned} M_{xy,\pm} &= \frac{\sqrt{3}}{4} \{ [h_{b'} \varepsilon_{x'x'} \cos(\phi + 2\varphi) \mp 2h_c \varepsilon_{x'z}'' \sin(2\phi + \varphi)] \\ &\quad + i [h_b \varepsilon_{x'x'} \sin 2(\phi - \varphi) \pm 2h_{c'} \varepsilon_{x'z}'' \cos(\phi - \varphi)] \}. \end{aligned} \quad (27)$$

After calculating $|M_{xy,\pm}|^2$, we obtain the transition rate

$$\begin{aligned} W_{xy,0} &\propto \langle \varepsilon_{x'x'}^2 [h_b^2 \sin^2 2\phi' + h_{b'}^2 \cos^2(\phi' + 3\varphi)] \\ &\quad + 4\varepsilon_{x'z}''^2 [h_c^2 \cos^2 \phi' + h_c^2 \sin^2(2\phi' + 3\varphi)] \end{aligned} \quad (28)$$

for $\eta = 0$. Here, ϕ' ($= \phi - \varphi$) is the field-rotation angle measured from the x' -axis.

To reveal the C_{3v} symmetry inherent in $W_{xy,0}$, we simplify Eq. (28) as

$$\begin{aligned} W_{xy,0} &\propto 2(1 + \lambda) + (1 + \lambda \cos 6\varphi)(\cos 2\phi' - \cos 4\phi') \\ &\quad + \lambda \sin 6\varphi(\sin 4\phi' - \sin 2\phi'), \end{aligned} \quad (29)$$

assuming that $\langle |h_{b'} \varepsilon_{x'x'}|^2 \rangle = \langle |2h_c \varepsilon_{x'z}''|^2 \rangle = \lambda \langle |h_b \varepsilon_{x'x'}|^2 \rangle = \lambda \langle |2h_{c'} \varepsilon_{x'z}''|^2 \rangle$. Here, the parameter λ represents a deviation from the spherical symmetric form of the spin–strain interaction. The last term in Eq. (29) describes the odd function nature of ϕ' . For $\lambda \neq 0$, this causes an asymmetric ϕ' depen-

dence with respect to the x' - and y' -axes. The amplitude of the asymmetry is proportional to $\sin 6\varphi$ and shows a periodic change with respect to each $\pi/3$, reflecting the C_{3v} symmetry. It vanishes for $\varphi = 0, \pm\pi/3, \pm2\pi/3$, and π , at which the SAW propagation direction merges to each mirror plane. The amplitude takes the maximum at $|\sin 6\varphi| = 1$, as shown for $\varphi = -\pi/12$ in Fig. 5, where we show how the ϕ' dependence of $W_{xy,0}$ for $\eta = 0$ is changed by increasing λ . The polar plot of the ϕ' dependence is symmetric in the spherical case $\lambda = 0$, which becomes twisted and asymmetric for $\lambda \neq 0$. Indeed, the indication of this behavior is inferred from the SAR measurements in SiC.³³⁾ The related comments are given in the next subsection. We emphasize that the twisted behavior cannot be understood by the spherical approximation because of the lack of information on the crystal structure; thus, the consideration of the C_{3v} symmetry is required for the V_{Si} spin-strain interaction, as proposed by the present theory.

3.7 Asymmetric field-direction dependence of SAR

Besides the single quantum spin transitions with $\Delta m_S = \pm 1$, the double quantum spin transitions with $\Delta m_S = \pm 2$ were also probed by the SAR measurements under a lower magnetic field. In Appendix C, we describe the calculation of the latter transition rate and the effect of SAW propagating in general directions on its asymmetric field-direction dependence. Comparing the observed $\Delta m_S = \pm 2$ SAR data³³⁾ with the calculated ones, we find a possibility that the SAW propagation direction is tilted counterclockwise ($\varphi > 0$ measured from the x -axis). To explain the asymmetric behavior of the $\Delta m_S = \pm 1$ SAR data,³³⁾ the coupling-strength ratio of the spin-strain interaction is required to satisfy $|h_{b'}/h_c| \ll 1$. With these conditions, both the $\Delta m_S = \pm 1$ and $\Delta m_S = \pm 2$ data can be simultaneously reproduced. Thus, it is worth checking whether the SAW propagation direction is actually tilted from the crystallographic mirror plane by more precise SAR measurements of the asymmetric field-direction dependence.

4. Conclusion

In this paper, we elaborated on the $S = 3/2$ V_{Si} spin-strain interaction considering the C_{3v} site symmetry for more detailed investigations of SAR under the rotation of a magnetic field. In our formulation, the ratios of coupling parameters, such as $h_{b'}/h_b$ and $h_{c'}/h_c$ in Eq. (3), can be evaluated from the field-direction dependence of the $\Delta m_S = \pm 1$ transition rate, although the effects of various local strain fields are included in the model Hamiltonian. Importantly, the anisotropic SAR exhibits a marked maximum of the transition rate reflecting the C_{3v} site symmetry of V_{Si} . This provides more detailed information on the quadrupole components of the spin-strain coupling beyond the spherical approximation. In this study, we demonstrated how to determine the model parameters listed in Table I to evaluate the coupling-strength ratios for C_{3v} from the observable SAR transition rates. Considering the $\Delta m_S = \pm 2$ transition rate as well, we also pointed out the deviation of the SAW propagation direction from the crystallographic mirror plane, which induces an additional anisotropy in the SAR transition rates peculiar to the C_{3v} symmetry. These results will promote a thorough analysis of the spin-strain coupling to realize the acoustic control of spin.

It is also important to confirm the applicability of the coupling parameters determined by our method to other ex-

periments such as optical measurements using static stress fields.³⁾ When a uniaxial or shear stress is applied, the induced local strain field changes the $S = 3/2$ energy levels of V_{Si} . Considering the spin-strain interaction Hamiltonian for the static strain field as presented here, we can estimate the energy level shifts, which can be measured by electron spin resonance using a microwave under a sufficiently strong stress to resolve each energy shift.

We would like to make a comment on the coupling parameters $h_{b'}$ and $h_{c'}$ related to the zx and yz quadrupole components. As argued in Sect. 3.5, for the NV centers in diamond, it has been presumably considered that the spin-strain coupling with $h_{b'}$ and $h_{c'}$ is less dominant than the coupling with h_b and h_c related to the $x^2 - y^2$ and xy quadrupole components. It is still unclarified whether the former coupling parameters could be measurable. On the other hand, the SAR measurement methods have been much more advanced for V_{Si} than for the NV centers. By applying our method to the SAR measurements, one can feasibly quantify the unknown $h_{b'}/h_b$ and $h_{c'}/h_c$ parameters for V_{Si} . As mentioned in Sect. 3.7, the anisotropic SAR shows some important indications owing to the effect of the C_{3v} symmetry, and the dominant coupling parameters can be identified by our theory when sufficient SAR data are accumulated.

The Si vacancy centers have attracted more attention in relation to multiquantum transitions such as multiphoton absorption processes in the $S = 3/2$ energy levels, which have recently been observed by measurements of optically detected magnetic resonance.²¹⁾ This finding will stimulate a challenging investigation of multiphonon-driven quantum spin transitions as the counterparts of multiphoton-driven transitions. It is also intriguing to extend our theory to the SAR associated with multiphonon absorption transitions.^{35,36)}

Acknowledgment This work was supported by JSPS KAKENHI Grant Number 21K03466.

Appendix A: Spin and quadrupole operators for spin-3/2

On the $|m_S\rangle$ basis for spin-3/2, $\{|3/2\rangle, |1/2\rangle, |-1/2\rangle, |-3/2\rangle\}$, the spin operators are explicitly given by the 4×4 matrices:

$$\begin{aligned} S_x &= \frac{1}{2} \begin{pmatrix} 0 & \sqrt{3} & 0 & 0 \\ \sqrt{3} & 0 & 2 & 0 \\ 0 & 2 & 0 & \sqrt{3} \\ 0 & 0 & \sqrt{3} & 0 \end{pmatrix}, \\ S_y &= \frac{1}{2} \begin{pmatrix} 0 & -i\sqrt{3} & 0 & 0 \\ i\sqrt{3} & 0 & -i2 & 0 \\ 0 & i2 & 0 & -i\sqrt{3} \\ 0 & 0 & i\sqrt{3} & 0 \end{pmatrix}, \\ S_z &= \frac{1}{2} \begin{pmatrix} 3 & 0 & 0 & 0 \\ 0 & 1 & 0 & 0 \\ 0 & 0 & -1 & 0 \\ 0 & 0 & 0 & -3 \end{pmatrix}. \end{aligned} \quad (\text{A}\cdot 1)$$

Using these matrices, we drive the quadrupole operators as

$$O_u = \sqrt{3} \begin{pmatrix} 1 & 0 & 0 & 0 \\ 0 & -1 & 0 & 0 \\ 0 & 0 & -1 & 0 \\ 0 & 0 & 0 & 1 \end{pmatrix},$$

$$\begin{aligned}
 O_v &= \sqrt{3} \begin{pmatrix} 0 & 0 & 1 & 0 \\ 0 & 0 & 0 & 1 \\ 1 & 0 & 0 & 0 \\ 0 & 1 & 0 & 0 \end{pmatrix}, \\
 O_{zx} &= \sqrt{3} \begin{pmatrix} 0 & 1 & 0 & 0 \\ 1 & 0 & 0 & 0 \\ 0 & 0 & 0 & -1 \\ 0 & 0 & -1 & 0 \end{pmatrix}, \\
 O_{xy} &= \sqrt{3} \begin{pmatrix} 0 & 0 & -i & 0 \\ 0 & 0 & 0 & -i \\ i & 0 & 0 & 0 \\ 0 & i & 0 & 0 \end{pmatrix}, \\
 O_{yz} &= \sqrt{3} \begin{pmatrix} 0 & -i & 0 & 0 \\ i & 0 & 0 & 0 \\ 0 & 0 & 0 & i \\ 0 & 0 & -i & 0 \end{pmatrix}. \quad (\text{A}\cdot 2)
 \end{aligned}$$

Let us consider the unitary transformation from $\mathcal{S} = (S_x, S_y, S_z)$ to $\mathcal{S}_B = (S_X, S_Y, S_Z)$,

$$U^\dagger(\mathbf{e}_\lambda \cdot \mathcal{S})U = S_\lambda \quad (\lambda = X, Y, Z), \quad (\text{A}\cdot 3)$$

where the matrix representations of S_X , S_Y , and S_Z in the (XYZ) frame are given as S_x , S_y , and S_z in Eq. (A-1), respectively. We choose $\mathbf{e}_X = (-\cos\theta\cos\phi, -\cos\theta\sin\phi, \sin\theta)$, $\mathbf{e}_Y = (\sin\phi, -\cos\phi, 0)$, and $\mathbf{e}_Z = (\sin\theta\cos\phi, \sin\theta\sin\phi, \cos\theta)$ for the magnetic field $\mathbf{B} \parallel Z$. Accordingly, the explicit form of the unitary matrix U is given as

$$U = \begin{pmatrix} \chi^{-3}cc_{a+} & \chi^{-3}c\tilde{s} & \chi^{-3}s\tilde{s} & \chi^{-3}sc_{a-} \\ \chi^{-1}c\tilde{s} & \chi^{-1}cc_{b-} & -\chi^{-1}sc_{b+} & -\chi^{-1}s\tilde{s} \\ \chi s\tilde{s} & -\chi sc_{b+} & -\chi cc_{b-} & \chi c\tilde{s} \\ \chi^3sc_{a-} & -\chi^3s\tilde{s} & \chi^3c\tilde{s} & -\chi^3cc_{a+} \end{pmatrix}. \quad (\text{A}\cdot 4)$$

Here, each matrix element consists of the following terms:

$$\begin{aligned}
 \chi &= e^{i\phi/2}, \quad c = \cos\frac{\theta}{2}, \quad s = \sin\frac{\theta}{2}, \quad \tilde{s} = \frac{\sqrt{3}}{2}\sin\theta, \\
 c_{a\pm} &= \frac{1 \pm \cos\theta}{2}, \quad c_{b\pm} = \frac{1 \pm 3\cos\theta}{2}. \quad (\text{A}\cdot 5)
 \end{aligned}$$

In the acoustically driven spin transitions, $S = 3/2$ states are coupled via the quadrupole components $\{O_u, O_v, O_{zx}, O_{xy}, O_{yz}\}$. For the rotation of a magnetic field, it is convenient to use the quadrupole operators in the (XYZ) frame, and the above unitary transformation gives

$$\begin{aligned}
 U^\dagger O_u U &= -\frac{1-3\cos^2\theta}{2}O_U + \frac{\sqrt{3}}{2}\sin^2\theta O_V \\
 &\quad + \sqrt{3}\sin\theta\cos\theta O_{ZX}, \\
 U^\dagger O_v U &= \left(\frac{\sqrt{3}}{2}\sin^2\theta O_U + \frac{1+\cos^2\theta}{2}O_V - \sin\theta\cos\theta O_{ZX} \right) \\
 &\quad \times \cos 2\phi \\
 &\quad + (-\cos\theta O_{XY} + \sin\theta O_{YZ})\sin 2\phi, \\
 U^\dagger O_{zx} U &= (\sqrt{3}\sin\theta\cos\theta O_U - \sin\theta\cos\theta O_V - \cos 2\theta O_{ZX}) \\
 &\quad \times \cos\phi \\
 &\quad + (\sin\theta O_{XY} + \cos\theta O_{YZ})\sin\phi, \\
 U^\dagger O_{xy} U &= \left(\frac{\sqrt{3}}{2}\sin^2\theta O_U + \frac{1+\cos^2\theta}{2}O_V - \sin\theta\cos\theta O_{ZX} \right)
 \end{aligned}$$

$$\begin{aligned}
 &\quad \times \sin 2\phi \\
 &\quad + (\cos\theta O_{XY} - \sin\theta O_{YZ})\cos 2\phi, \\
 U^\dagger O_{yz} U &= (\sqrt{3}\sin\theta\cos\theta O_U - \sin\theta\cos\theta O_V - \cos 2\theta O_{ZX}) \\
 &\quad \times \sin\phi \\
 &\quad + (-\sin\theta O_{XY} - \cos\theta O_{YZ})\cos\phi. \quad (\text{A}\cdot 6)
 \end{aligned}$$

Here, the matrices of the quadrupole operators O_K ($K = U, V, ZX, XY, YZ$) are constructed by the components of \mathcal{S}_B and given by the same representations of O_k ($k = u, v, zx, xy, yz$) in Eq. (A-2), respectively. The unitary transformation $U^\dagger O_k U$ is represented by a linear combination of the five components O_K . Accordingly, we obtain $H_{\varepsilon, B} = U^\dagger H_\varepsilon U \equiv \sum_K A_{K, \varepsilon} O_K$ in Eq. (4), where $A_{K, \varepsilon}$ depends on the field direction represented by θ and ϕ .

Appendix B: Spherically symmetric spin–strain interaction model

A spherically symmetric form of the spin–strain interaction is simply described by the following Hamiltonian:

$$\begin{aligned}
 H_\varepsilon^s &= \xi \sum_{\alpha, \beta = x, y, z} \varepsilon_{\alpha\beta} S_\alpha S_\beta \\
 &= \xi \left[\frac{1}{2}(\varepsilon_u O_u + \varepsilon_v O_v) + \varepsilon_{yz} O_{yz} + \varepsilon_{zx} O_{zx} + \varepsilon_{xy} O_{xy} \right], \quad (\text{B}\cdot 1)
 \end{aligned}$$

where the coupling constant is given by a single parameter ξ , and the term of a bulk strain component is not written. In a similar form in Eq. (1), the strain-dependent coupling coefficients in $H_\varepsilon^s = \sum_k A_{k, \varepsilon}^s O_k$ are written as

$$\begin{aligned}
 A_{u, \varepsilon}^s &= \frac{\xi}{2}\varepsilon_u, \quad A_{v, \varepsilon}^s = \frac{\xi}{2}\varepsilon_v, \quad A_{zx, \varepsilon}^s = \xi\varepsilon_{zx}, \\
 A_{xy, \varepsilon}^s &= \xi\varepsilon_{xy}, \quad A_{yz, \varepsilon}^s = \xi\varepsilon_{yz}. \quad (\text{B}\cdot 2)
 \end{aligned}$$

Comparing these $A_{k, \varepsilon}^s$ and $A_{k, \varepsilon}$ in Eq. (3), we can characterize the spherical symmetry of the spin–strain interaction by the coupling parameters for C_{3v} as

$$h_a = h_b = h_c = 2\xi, \quad h_c = h_{b'} = 0. \quad (\text{B}\cdot 3)$$

Thus, a deviation from the spherical symmetry is expressed by finite h_c and $h_{b'}$. For the $\pm x$ propagating SAWs we considered here, h_c in $A_{v, \varepsilon}$ is related to the $x^2 - y^2$ quadrupole component coupled to the ε_{zx} field, whereas $h_{b'}$ in $A_{zx, \varepsilon}$ is related to the zx quadrupole component coupled to the $\varepsilon_v (= \varepsilon_{xx})$ field. Assuming that ε_{xx} is real and $\varepsilon_{zx} \equiv -i\varepsilon_{zx}''$ for a plane Rayleigh SAW, we treat $A_{v, \varepsilon}$ and $A_{zx, \varepsilon}$ as complex numbers for C_{3v} ,

$$\begin{aligned}
 |A_v|e^{i\theta_v} &= \frac{1}{2} \left(\frac{1}{2}h_b\varepsilon_{xx} + ih_c\varepsilon_{zx}'' \right), \\
 |A_{zx}|e^{i\theta_{zx}} &= \frac{1}{2} \left(-\frac{1}{2}h_{b'}\varepsilon_{xx} - ih_{c'}\varepsilon_{zx}'' \right), \quad (\text{B}\cdot 4)
 \end{aligned}$$

which lead to Eq. (6). One can find that $\theta_v = 0$ and $|\theta_{zx}| = \pi/2$ for the spherical spin–strain coupling in Eq. (B-3). Thus, it is also useful to represent a deviation from the spherical symmetry by $|\theta_v|$ and $(\pi/2 - |\theta_{zx}|)$ instead of h_c and $h_{b'}$, respectively.

In the spherical model, for the inplane (xy) field rotation, the ϕ dependence of the transition rate W_{xy} ($\eta = 0$) is almost the same as that observed in Fig. 2(b) for the C_{3v} site sym-

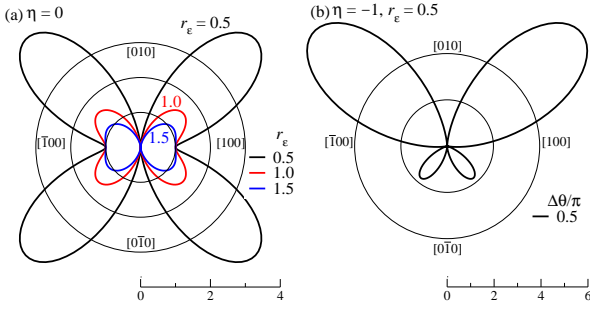


Fig. B-1. (Color online) Field-direction ϕ dependence of the transition rate W_{xy} in the spherical case. (a) Polar representation of the normalized rate for $\eta = 0$. The data are plotted for $r_\varepsilon \equiv 2\langle|\varepsilon''_{zx}\varepsilon_{xx}|\rangle/\langle\varepsilon''_{xx}\rangle = 0.5, 1.0, \text{ and } 1.5$. (b) Polar representation of the normalized rate for $\eta = -1$, where $r_\varepsilon = 0.5$ and $\Delta\theta/\pi \equiv (\theta_{zx} - \theta_v)/\pi = 0.5$.

metry. The only difference is that $\langle|a_{zx}|\rangle$ does not contain the coupling parameters but is only strain-dependent as

$$\langle|a_{zx}|\rangle = \frac{\langle|A_{zx,\varepsilon}^s||A_{v,\varepsilon}^s|\rangle}{\langle|A_{v,\varepsilon}^s|^2\rangle} = 2\frac{\langle|\varepsilon''_{zx}\varepsilon_{xx}|\rangle}{\langle\varepsilon''_{xx}\rangle} \quad (\text{spherical}), \quad (\text{B}\cdot 5)$$

where Eq. (B-2) is used. To compare the spherically symmetric and C_{3v} symmetric models, we show W_{xy} in Fig. B-1(a) by replacing $\langle|a_{zx}|\rangle$ with $r_\varepsilon \equiv 2\langle|\varepsilon''_{zx}\varepsilon_{xx}|\rangle/\langle\varepsilon''_{xx}\rangle$ (see Fig. 2(b) for comparison). Note that the V-shaped angular dependence cannot be obtained for $r_\varepsilon \gtrsim 1$ in the spherical case ($h_b = h_{c'}$). Applying a similar argument to W_{xy} for $|\eta| = 1$ discussed in Sect. 3.3, we show a polar plot for the spherical model in Fig. B-1(b). This is the same as the plot for $\Delta\theta/\pi = 0.5$ in Fig. 3(b), where $\langle|a_{zx}|\rangle = 0.5$ is replaced by $r_\varepsilon = 0.5$.

Appendix C: Double quantum spin transition by SAW

C.1 Transition rate under inplane (xy) field rotation

In our formulation, the $\Delta m_S = \pm 2$ transition matrix element is calculated by the quadrupole coupling operator $A_{v,\varepsilon}O_v + A_{X,Y,\varepsilon}O_{XY}$ in Eq. (4). By analogy with Eq. (9), we represent the double quantum spin transition rate for the inplane (xy) field rotation as

$$W_{xy}^{(2)} \propto \left\langle \frac{3}{4}|A_v|^2 \left[(3a_u^2 + 2\sqrt{3}a_u \cos \theta_v \cos 2\phi + \cos^2 2\phi) + 4|a_{zx}|^2 \sin^2 \phi + 4\eta|a_{zx}| \left[\sqrt{3}a_u \sin \theta_{zx} + \sin(\theta_{zx} - \theta_v) \cos 2\phi \right] \sin \phi \right] \right\rangle, \quad (\text{C}\cdot 1)$$

where $a_u = A_u/|A_v|$ and $a_{zx} = |A_{zx}|/|A_v|$. The parameters θ_v and θ_{zx} characterize the complex numbers as $A_v = |A_v|e^{i\theta_v}$ and $A_{zx} = |A_{zx}|e^{i\theta_{zx}}$. In Fig. C-1(a), we show the polar representation of the normalized transition rate $W_{xy}^{(2)}/W_{xy,\phi=0}^{(2)}$ for $\eta = 0$ to compare the data for $|a_{zx}| = 0.5$ and 1.0 , which are the same parameters used in Fig. 2(b). We also adjust the values of $\langle a_u \rangle$ and $\cos \theta_v$ to satisfy $W_{xy,\phi=\pi/2}^{(2)}/W_{xy,\phi=0}^{(2)} = 2$ here. As a function of ϕ , these transition rates are explicitly written as

$$W_{xy,\eta=0}^{(2)}(\langle|a_{zx}|\rangle = 0.5) \propto \frac{3}{4}(\cos^2 2\phi + \sin^2 \phi), \quad (\text{C}\cdot 2)$$

$$W_{xy,\eta=0}^{(2)}(\langle|a_{zx}|\rangle = 1.0) \propto \frac{3}{4} \left(1 + \frac{2}{3} \cos 2\phi + \cos^2 2\phi + 4 \sin^2 \phi \right). \quad (\text{C}\cdot 3)$$

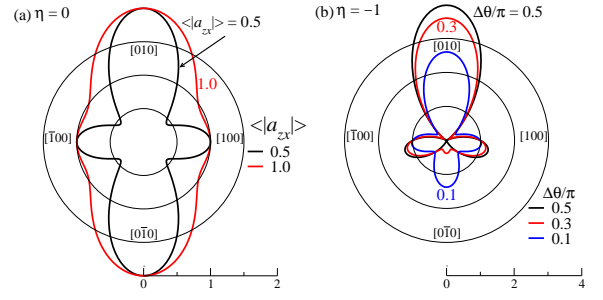


Fig. C-1. (Color online) Polar representation of $W_{xy}^{(2)}/W_{xy,\phi=0}^{(2)}$ for $\Delta m_S = \pm 2$ plotted with respect to the field direction ϕ . (a) Standing SAW case ($\eta = 0$) plotted for $\langle|a_{zx}|\rangle = 0.5$ and 1.0 . (b) Traveling SAW case ($\eta = -1$) plotted for $\Delta\theta \equiv (\theta_{zx} - \theta_v)/\pi = 0.5, 0.3, \text{ and } 0.1$, where we choose $\langle|a_{zx}|\rangle$ and fix $\langle a_u \rangle = 0$.

Note that the four minima of $W_{xy}^{(2)}$ become prominent with the decrease in $|a_{zx}|$ from unity, and this cross-shaped angular dependence indicates $|h_{c'}/h_b| < 1$ for the spin-strain coupling.

In Eq. (C-1), $W_{xy}^{(2)}$ for $\eta \neq 0$ shows an asymmetric ϕ dependence with respect to the x -axis, which depends on $\Delta\theta$ ($\equiv \theta_{zx} - \theta_v$) when we fix $\langle a_u \rangle \propto \langle A_u|A_v| \rangle = 0$. In Fig. C-1(b), the normalized transition rate is plotted for $\eta = -1$ and $\langle|a_{zx}|\rangle = 0.5$, where the parameters are changed in the same way as in Fig. 3(b). For $\Delta\theta = 0$, $W_{xy}^{(2)}$ is reduced to Eq. (C-2) and shows the symmetric ϕ dependence for $\langle|a_{zx}|\rangle = 0.5$ in Fig. C-1(a). In Fig. C-1(b), a prominent feature of $W_{xy,\eta=-1}^{(2)}$ is its marked dependence on $\Delta\theta$ at $\phi = \pi/2$ (in the upper xy plane).

For the spherical model in Eq. (B-1), the ϕ dependence for $|\eta| = 1$ corresponds to $\Delta\theta/\pi = 0.5$. For a large deviation $|\Delta\theta/\pi| \ll 0.5$ from the spherical symmetry, the ϕ dependence becomes symmetric, and this behavior is similar to that observed in Fig. 2(b) for the single quantum spin transition.

C.2 SAW propagating in general directions

In this subsection, we apply a similar argument in Sect. 3.6 to the field-direction dependence of the $\Delta m_S = \pm 2$ transition rate. First, we generalize Eq. (29) for the $\Delta m_S = \pm 1$ transition rate as

$$W_{xy,0} \propto 2 + \lambda_c + \lambda_{b'} + (1 + \lambda_{b'} \cos 6\phi) \cos 2\phi' - (1 + \lambda_c \cos 6\phi) \cos 4\phi' + \sin 6\phi(\lambda_c \sin 4\phi' - \lambda_{b'} \sin 2\phi'), \quad (\text{C}\cdot 4)$$

under the conditions of $\langle|h_b\varepsilon_{x'x'}|^2\rangle = \lambda_{b'}\langle|h_b\varepsilon_{x'x'}|^2\rangle$, $\langle|h_c\varepsilon_{x'z'}^2\rangle = \lambda_c\langle|h_c\varepsilon_{x'z'}^2\rangle$, and $\langle|h_b\varepsilon_{x'x'}|^2\rangle = \langle|2h_{c'}\varepsilon_{x'z'}^2\rangle$ in Eq. (28). On the other hand, the $\Delta m_S = \pm 2$ transition rate for $\eta = 0$ is given by

$$W_{xy,0}^{(2)} \propto \left\langle [h_a(\varepsilon_{zz} - \varepsilon_{x'x'}/2) + (h_b\varepsilon_{x'x'}/2) \cos 2\phi']^2 + 4h_{c'}^2\varepsilon_{x'z'}^2 \sin^2 \phi' + h_{b'}^2\varepsilon_{x'x'}^2 \sin^2(\phi' + 3\phi) + h_c^2\varepsilon_{x'z'}^2 \cos^2(2\phi' + 3\phi) \right\rangle. \quad (\text{C}\cdot 5)$$

Using the same conditions of the strain-dependent coupling parameters $\lambda_{b'}$ and λ_c in Eq. (C-4), we can reduce it to

$$W_{xy,0}^{(2)} \propto \frac{5}{4} + \frac{5}{8}(\lambda_c + \lambda_{b'}) - \frac{1}{2}(1 + 2\lambda_{b'} \cos 6\phi) \cos 2\phi' + \frac{1}{4}(1 + \lambda_c \cos 6\phi) \cos 4\phi'$$

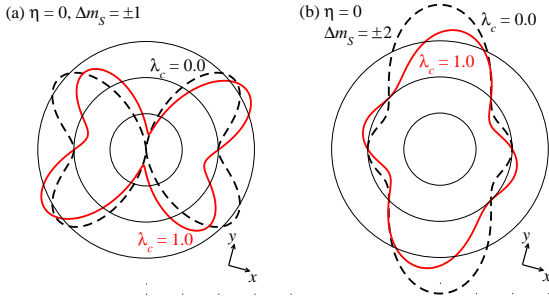


Fig. C-2. (Color online) Polar representation of the normalized transition rate for $\eta = 0$. (a) $W_{xy,0}/W_{xy,0,\phi'=0}$ for $\Delta m_S = \pm 1$ in Eq. (C-4). (b) $W_{xy,0}^{(2)}/W_{xy,0,\phi'=0}^{(2)}$ for $\Delta m_S = \pm 2$ in Eq. (C-6). Here, the SAW propagation (horizontal) direction is tilted counterclockwise by $\varphi = \pi/12$ from the x -axis of the crystal. The angular ϕ' dependence is plotted for $\lambda_c = 0.0$ and 1.0 , where $\lambda_{b'} = 0$ is fixed.

$$+ \frac{1}{4} \sin 6\varphi (4\lambda_{b'} \sin 2\phi' - \lambda_c \sin 4\phi'). \quad (\text{C-6})$$

Here, we have also assumed that $\langle |h_a(\epsilon_{zz} - \epsilon_{x'x'}/2)|^2 \rangle = 0$ and $\langle 4h_a h_b \epsilon_{x'x'}(\epsilon_{zz} - \epsilon_{x'x'}/2) \rangle = \langle |h_b \epsilon_{x'x'}|^2 \rangle$ to satisfy $W_{xy,0,\phi'=\pi/2}^{(2)}/W_{xy,0,\phi'=0}^{(2)} = 2$ for $\lambda_c = \lambda_{b'} = 0$.

In Eqs. (C-4) and (C-6), the odd function terms of ϕ' bring about an asymmetric ϕ' dependence with respect to the x' - and y' -axes. We find that $\sin 6\varphi > 0$ reproduces the observed field-direction dependence of the $\Delta m_S = \pm 2$ transition in SiC.³³⁾ Here, $\varphi > 0$ denotes that the SAW propagation direction is tilted counterclockwise. On the other hand, $\sin 6\varphi < 0$ is inferred from the $\Delta m_S = \pm 1$ data.³³⁾ Unless $\lambda_{b'}$ is extremely small in the $\sin 2\phi'$ term, the observed field-direction dependence can be identified in Fig. 5. In other words, $\lambda_{b'} \ll \lambda_c$ is required to reproduce this asymmetric behavior when $\varphi > 0$ is adopted for the SAW propagation direction.

In Fig. C-2(a), we show the polar representation of $W_{xy,0}$ for $\Delta m_S = \pm 1$ in Eq. (C-4) to demonstrate how the effect of the $\sin 4\phi'$ term appears as the asymmetric ϕ' dependence of $W_{xy,0}$. Here, we compare the results of $\lambda_c = 0.0$ and 1.0 in the absence of the $\sin 2\phi'$ term ($\lambda_{b'} = 0$). Figure C-2(b) shows the plot of $W_{xy,0}^{(2)}$ for $\Delta m_S = \pm 2$ in Eq. (C-6). From these results, we can consider that the observed SAR data indicate $|h_{b'}/h_c| \ll 1$ for the spin-strain coupling, and a finite h_c dominates the deviation from the spherical symmetry in the spin-strain interaction.

1) J. H. Van Vleck, Phys. Rev. **57**, 426 (1940).
 2) P. L. Donoho, Phys. Rev. **133**, A1080 (1964).
 3) P. Udvarhelyi, V. O. Shkolnikov, A. Gali, G. Burkard, and A. Pályi, Phys. Rev. B **98**, 075201 (2018).
 4) K. V. Kepesidis, S. D. Bennett, S. Portolan, M. D. Lukin, and P. Rabl, Phys. Rev. B **88**, 064105 (2013).
 5) E. R. MacQuarrie, T. A. Gosavi, N. R. Jungwirth, S. A. Bhave, and G. D. Fuchs, Phys. Rev. Lett. **111**, 227602 (2013).
 6) P. Ovarthaiyapong, K. W. Lee, B. A. Myers, and A. C. Bleszynski Jayich, Nat. Commun. **5**, 4429 (2014).
 7) E. R. MacQuarrie, T. A. Gosavi, A. M. Moehle, N. R. Jungwirth, S. A.

Bhave, and G. D. Fuchs, Optica **2**, 233 (2015).
 8) A. Barfuss, J. Teissier, E. Neu, A. Nunnenkamp, and P. Maletinsky, Nat. Phys. **11**, 820 (2015).
 9) S. Meesala, Y.-I. Sohn, H. A. Atikian, S. Kim, M. J. Burek, J. T. Choy, and M. Lončar, Phys. Rev. Appl. **5**, 034010 (2016).
 10) D. A. Golter, T. Oo, M. Amezcua, K. A. Stewart, and H. Wang, Phys. Rev. Lett. **116**, 143602 (2016).
 11) D. Lee, K. W. Lee, J. V. Cady, P. Ovarthaiyapong, and A. C. Bleszynski Jayich, J. Opt. **19**, 033001 (2017).
 12) C. L. Degen, F. Reinhard, and P. Cappellaro, Rev. Mod. Phys. **89**, 035002 (2017).
 13) H. Y. Chen, E. R. MacQuarrie, and G. D. Fuchs, Phys. Rev. Lett. **120**, 167401 (2018).
 14) A. Barfuss, M. Kasperczyk, J. Kölbl, and P. Maletinsky, Phys. Rev. B **99**, 174102 (2019).
 15) J. F. Barry, J. M. Schloss, E. Bauch, M. J. Turner, C. A. Hart, L. M. Pham, and R. L. Walsworth, Rev. Mod. Phys. **92**, 015004 (2020).
 16) H. Y. Chen, S. A. Bhave, and G. D. Fuchs, Phys. Rev. Appl. **13**, 054068 (2020).
 17) V. A. Norman, S. Majety, Z. Wang, W. H. Casey, N. Curro, and M. Radulaski, InfoMat. **3**, 869 (2021).
 18) S. J. Whiteley, G. Wolfowicz, C. P. Anderson, A. Bourassa, H. Ma, M. Ye, G. Koolstra, K. J. Satzinger, M. V. Holt, F. J. Heremans, A. N. Cleland, D. I. Schuster, G. Galli, and D. D. Awschalom, Nat. Phys. **15**, 490 (2019).
 19) V. A. Soltamov, C. Kasper, A. V. Poshakinskiy, A. N. Anisimov, E. N. Mokhov, A. Sperlich, S. A. Tarasenko, P. G. Baranov, G. V. Astakhov, and V. Dyakonov, Nat. Commun. **10**, 1678 (2019).
 20) S. J. Whiteley, F. J. Heremans, G. Wolfowicz, D. D. Awschalom, and M. V. Holt, Nat. Commun. **10**, 3386 (2019).
 21) H. Singh, M. A. Hollberg, A. N. Anisimov, P. G. Baranov, and D. Suter, Phys. Rev. Res. **4**, 023022 (2022).
 22) N. Mizuochi, S. Yamasaki, H. Takizawa, N. Morishita, T. Ohshima, H. Itoh, and J. Isoya, Phys. Rev. B **68**, 165206 (2003).
 23) J. Isoya, T. Umeda, N. Mizuochi, N. T. Son, E. Janzén, and T. Ohshima, Phys. Status Solidi B **245**, 1298 (2008).
 24) D. Simin, V. A. Soltamov, A. V. Poshakinskiy, A. N. Anisimov, R. A. Babunts, D. O. Tolmachev, E. N. Mokhov, M. Trupke, S. A. Tarasenko, A. Sperlich, P. G. Baranov, V. Dyakonov, and A. Astakhov, Phys. Rev. X **6**, 031014 (2016).
 25) Ö. O. Soykal and T. L. Reinecke, Phys. Rev. B **95**, 081405(R) (2017).
 26) S. A. Tarasenko, A. V. Poshakinskiy, D. Simin, V. A. Soltamov, E. N. Mokhov, P. G. Baranov, V. Dyakonov, and G. V. Astakhov, Phys. Status Solidi B **255**, 1700258 (2018).
 27) A. V. Poshakinskiy and G. V. Astakhov, Phys. Rev. B **100**, 094104 (2019).
 28) S. Castelletto and A. Boretti, J. Phys.: Photonics **2**, 022001 (2020).
 29) D. V. Sosnovsky and K. L. Ivanov, Phys. Rev. B **103**, 014403 (2021).
 30) A. Hernández-Mínguez, A. V. Poshakinskiy, M. Hollenbach, P. V. Santos, and G. V. Astakhov, Sci. Adv. **7**, eabj5030 (2021).
 31) T. Vasselton, A. Hernández-Mínguez, M. Hollenbach, G. V. Astakhov, and P. V. Santos, Phys. Rev. Appl. **20**, 034017 (2023).
 32) J. R. Dietz, B. Jiang, A. M. Day, S. A. Bhave, and E. L. Hu, Nat. Electron. **6**, 739 (2023).
 33) A. Hernández-Mínguez, A. V. Poshakinskiy, M. Hollenbach, P. V. Santos, and G. V. Astakhov, Phys. Rev. Lett. **125**, 107702 (2020).
 34) I. D. Breev, A. V. Poshakinskiy, V. V. Yakovleva, S. S. Nagalyuk, E. N. Mokhov, R. Hübner, G. V. Astakhov, P. G. Baranov, and A. N. Anisimov, Appl. Phys. Lett. **118**, 084003 (2021).
 35) M. Koga and M. Matsumoto, J. Phys. Soc. Jpn. **89**, 113701 (2020).
 36) M. Koga and M. Matsumoto, J. Phys. Soc. Jpn. **91**, 094709 (2022).
 37) P. Udvarhelyi and A. Gali, Phys. Rev. Appl. **10**, 054010 (2018).
 38) P. Kehayias, M. J. Turner, R. Trubko, J. M. Schloss, C. A. Hart, M. Wesson, D. R. Glenn, and R. L. Walsworth, Phys. Rev. B **100**, 174103 (2019).